A Comprehensive Analysis of Eco-Friendly Cs_2SnI_6 Based Tin Halide Perovskite Solar Cell through Device Modeling

Debashish Pal

Abstract: The choice of appropriate materials is of paramount importance in realizing a high efficiency perovskite solar cell. Lead free eco-friendly perovskite solar cell architecture is theoretically investigated using solar cell capacitance simulator (SCAPS) for device performance. Preliminary investigations on Cs_2SnI_6 solar cell architectures have indicated that the presence of hole transport layer is crucial in achieving an open-circuit voltage greater than 0.6 V. The presence of a valence band offset between the Cs_2SnI_6 absorber and hole transport layer has a significant detrimental impact on the short-circuit current density and fill factor of the cell. A novel device architecture employing TiO_2 as an electron transport material and Cu_2O as a hole transport material is proposed to overcome the limitations associated with the current designs. Theoretical investigations are carried out employing 1D SCAPS simulation program in order to optimize the structure by varying the perovskite thickness, bandgap, and defect concentration. The proposed solar cell after optimization has a practically realizable power conversion efficiency of 17.77%.

1. Introduction

Solar photovoltaic technology continues to drive the growth in renewable energy demand across the globe in which silicon is the most commonly used semiconductor material accounting for more than 95% of the total worldwide production. Perovskite materials offer a number of advantages compared to traditional Si solar cells due to their direct energy bandgap, long diffusion length, low exciton binding energy, ambipolar charge transport, and high absorbance. Furthermore they can be developed through inexpensive solution processing techniques.[1–4] Researchers have dedicated considerable time and attention to finding a suitable alternative for lead-based perovskites primarily because of its long-term detrimental impact on the environment and human health. The tin-based perovskite material has emerged as a promising candidate to replace lead perovskite solar cells, currently presenting a maximum power conversion efficiency of 14.8%.[5–11] The tin-based perovskite materials do not offer long term stable operation because Sn^{2+} ions rapidly oxidizes to a more stable Sn^{4+} in the presence of air and moisture. Recently significant progress has been made in restricting the oxidation of Sn^{2+} ions with the development of encapsulation and fabrication methods.[12–14] Several first principles investigation have suggested that Cs_2SnI_6 double perovskite material can be utilized as an active material in prospective solar cell devices.[15–17]

A two-step modified deposition can yield high purity stable Cs_2SnI_6 films resulting in grain sizes ranging a few micrometers. The Cs_2SnI_6 double perovskite has a direct bandgap ranging from 1.3 to 1.37 eV, exhibiting n-type semiconducting nature with extremely high hole mobility (329 cm^2 V^{-1} s^{-1}) in iodine rich samples.[18] Cs_2SnI_6 films were obtained by employing a modified two-step process resulting in n-type semiconducting characteristics of with remarkably high carrier mobility (425 cm^2 V^{-1} s^{-1}) and bandgap ranging from 1.29 to 1.42 eV.[19] Double perovskite air-stable photoconductive films were reported to have an optical bandgap of 1.3 eV and open-circuit voltage of 0.86 V for inorganic FTO/CdS/Cs_2SnI_6/C/Ag solar cell configuration.[20] A power conversion efficiency of 0.86% was achieved for a mesoporous solar cell utilizing the FTO/ZnO seed layer/ZnO nanorods/Cs_2SnI_6/P3HT/Ag configuration where the Cs_2SnI_6 film reportedly had a bandgap of 1.48 eV. In this architecture the ZnO seed layer acted as the electron transport material, whereas the ZnO nanorods serve as the scaffold for Cs_2SnI_6 film.[21] High quality air-stable Cs_2SnI_6 thin film exhibited an extremely impressive absorption coefficient (>10^5 cm^{-1}) with a bandgap of 1.48 eV. This absorber material when employed in a FTO/TiO_2/Cs_2SnI_6/P3HT/Ag planar configuration demonstrated an encouraging power conversion efficiency of 0.96%.[22] A summary of the recent experimental findings for Cs_2SnI_6 solar cells using different architectures are shown in **Table 1**.

D. Pal
Department of Material Science and Engineering
Tripura University
Agartala 799022, India
E-mail: P.Debashish@napier.ac.uk

D. Pal
School of Computing
Engineering and the Built Environment
Edinburgh Napier University
Edinburgh EH10 5DT, UK

The ORCID identification number(s) for the author(s) of this article can be found under https://doi.org/10.1002/adts.202200856

Table 1. Brief summary of synthesis techniques and electrical outputs of Cs_2SnI_6 solar cells.

Structure	Device architecture	Synthesis route	V_{OC} [V]	J_{SC} [mA cm^{-2}]	FF [%]	PCE [%]	Refs.
A	FTO/CdS/Cs$_2$SnI$_6$/C/Ag	Solution	0.86	0.33	37.00	0.11	[20]
B	FTO/ZnO seed layer/ZnO nanorods/Cs$_2$SnI$_6$/P3HT/Ag	Solution	0.52	3.20	51.50	0.857	[21]
C	FTO/TiO$_2$/Cs$_2$SnI$_6$/P3HT/Ag	Evaporation	0.51	5.41	35.00	0.96	[22]
D	FTO/TiO$_2$/Cs$_2$SnI$_6$/P3HT/Ag	Solution	0.256	7.41	24.50	0.47	[23]
E	ITO/B-γ-CsSnI$_3$/Cs$_2$SnI$_6$/Au	Evaporation	0.63	6.10	28.40	1.10	[24]

Interestingly none of the fabricated Cs_2SnI_6 solar cells could achieve performance close to expectations, especially considering the reported bandgap which is favorable for light absorption. This can be attributed to a number of factors like long-term instability, hysteresis loss, morphology, grain size, grain boundaries, and the presence of interfacial defects.[25–34] Therefore it is apparent that there is no clear consensus on the practically achievable power conversion efficiency of Cs_2SnI_6 perovskite solar cells. Also there are scarce theoretical reports, which address the limitations encountered by Cs_2SnI_6 solar cells in achieving their full potential in power conversion. An optimized FTO/graphene oxide/Cs_2SnI_6/Cu_2O/Au configuration was employed to obtain maximum theoretical parameters of $V_{OC} = 0.837$ V, $J_{SC} = 34.6$ mA cm^{-2}, FF = 81.64%, and $\eta = 23.64\%$ considering a total 10^{14} cm^{-3} defect density.[35] A solar cell utilizing the same architecture, at the same defect concentration was demonstrated to have an optimum $V_{OC} = 1.0$ V, $J_{SC} = 25.93$ mA cm^{-2}, FF = 29.57%, and $\eta = 7.73\%$.[36] The discrepancies in theoretical results and experimental values should be tackled in order to gain an in-depth understanding of the physics behind the operation of perovskite material based solar cells.

Inspired by the discussions above we conducted a systematic and extensive theoretical investigation on the realistic power conversion efficiency achievable by Cs_2SnI_6-based perovskite thin film solar cell through numerical simulation. First, we used the materials and configurations already used in the experiments to obtain theoretically achievable electrical outputs and compared these results. Based on these results the limitations associated with the designs were discussed and a new architecture was proposed which would hopefully overcome the limitations of earlier configurations. To help us achieve this objective we employed the 1D solar cell capacitance simulator (SCAPS) program. We studied the effect of variation in thickness and bandgap of the Cs_2SnI_6 layer on the solar cell performance. In order to simulate a practically realizable device various defect states inside the absorber were also taken into consideration. The interfacial properties of the electron transport layer-perovskite and the perovskite-hole transport layer were also accounted for in the simulations. Furthermore we also demonstrated how the choice of a back metal contact, having appropriate work function can boost the electrical output of the proposed solar cell.

2. Methodology

SCAPS is an open source tool written in the C programming language for the simulation of thin film solar cells, which was designed and developed by the University of Ghent, Belgium.[37] SCAPS program employs the 1D drift-diffusion model to solve

the Poisson's and continuity equations together with the boundary conditions to give an accurate description of the internal electric field and the movement of electrons and holes inside the device. The equations can be represented mathematically as

$$\frac{\partial}{\partial x}\left(\varepsilon(x)\frac{\partial\varphi}{\partial x}\right) = -q\left[-p(x) + n(x) - N_D^+(x) + N_A^-(x) + \rho_n - \rho_p\right] \tag{1}$$

$$\frac{\partial J_n}{\partial x} = q\left(R_n - G + \frac{\partial n}{\partial t}\right) \tag{2}$$

$$\frac{\partial J_p}{\partial x} = -q\left(R_p - G + \frac{\partial p}{\partial t}\right) \tag{3}$$

$$J_n = nq\mu_n\frac{\partial\varphi}{\partial x} + qD_n\frac{\partial n}{\partial x} \tag{4}$$

$$J_p = pq\mu_p\frac{\partial\varphi}{\partial x} - qD_p\frac{\partial p}{\partial x} \tag{5}$$

where φ is the potential, ϵ is permittivity, q is electronic charge, p is free hole concentration, n is free electron concentration, N_D^+ is donor ion concentration, N_A^- is acceptor ion concentration, ρ_n is the electron defect distribution, ρ_p is the hole defect distribution, J_n is electron current density, J_p is hole current density, R_n is electron recombination rate, R_p is hole recombination rate, G is the charge generation rate, μ_n is electron mobility, μ_p is hole mobility, D_n is diffusivity of electrons, and D_p is the diffusivity of holes. For the calculation of the absorption coefficient a model corresponding to the following equation was adopted

$$\alpha(\lambda) = \left(A + \frac{B}{h\upsilon}\right)\sqrt{h\upsilon - E_g} \tag{6}$$

where A and B are constants, h is the plank constant, υ is the frequency of photons, and E_g is the energy bandgap of the material.

In this investigation, all simulations were carried out at room temperature (300 K) and AM1.5G illumination with an intensity of 1000 W m^{-2}. Additionally, the surface recombination velocities of electrons and holes at the front and back contacts were also held constant at 10^7 cm s^{-1}. Furthermore, in order to emulate a realistic device and for the sake of computational simplicity the light reflection at the front and back contacts were ignored.

3. Device Architecture and Input Parameters

An all-inorganic device structure comprising of TiO_2 as an electron transport layer and Cu_2O as a hole transport layer has been

2200856 (2 of 10)

ADVANCED
SCIENCE NEWS
www.advancedsciencenews.com

ADVANCED
THEORY AND
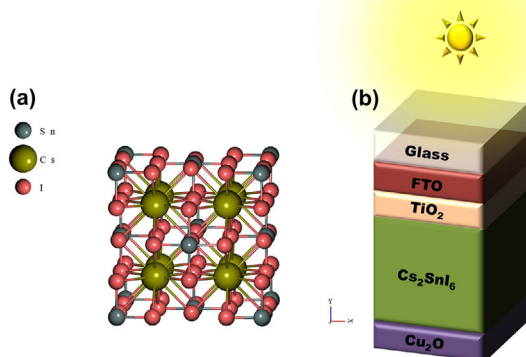SIMULATIONS
www.advtheorysimul.com

Figure 1. a) Crystal structure of Cs_2SnI_6 double perovskite and b) proposed Cs_2SnI_6 solar cell architecture.

proposed (**Figure 1**) based on the results of initial investigations on the already existing configurations reported in experiments shown in Table 1. The outcomes of these simulations have been discussed in the subsequent section. The initial proposed structure has material parameters, which are listed in **Table 2**, layer defects in **Table 3**, and interfacial defects described in **Table 4**. All the essential parameters used in this theoretical study have been derived from existing literature as follows: $FTO,^{[38]}$ $TiO_2,^{[39]}$ $Cs_2SnI_6,^{[35,36,40–42]}$ and $Cu_2O.^{[43,44]}$ Moreover the other material parameters used for ZnO, CdS, and P3HT in the simulation have been summarized in Table S1 of the Supporting Information.

4. Initial Analysis

During the initial assessment it was found that the solar cell configurations used in the experiments had yielded electrical outputs which were very inferior in terms of performance when compared to the simulation results. It is worthy of mention that the factors listed in Tables 3 and 4 were also taken into account when simulating the experimental solar cell architectures. Nevertheless, the disparity in the simulated and experimental study could be ascribed to several factors especially the choice of materials, since they can induce structural discontinuity, interfacial incompatibility having inconsistent grain sizes and boundaries. Furthermore, the different values of electron affinity and bandgap of materials can give rise to unfavorable conduction and valence band offsets resulting in the obstruction of electron and hole transport. One particularly noteworthy finding when Table 1 and Figure S1 of the Supporting Information are compared, is the very low values of short-circuit current density (J_{SC}) reported in the experiments. Therefore in order to have a fair comparison, a standard Cs_2SnI_6 solar cell configuration was proposed, with TiO_2 as electron transport layer and Cu_2O as the hole transport layer, already discussed in the last section. A low value of J_{SC} is indicative of higher recombination rate of electrons and holes, which can be elucidated by examining the energy band diagram and the charge carrier recombination profile across the device, as shown in Figures S2 and S3 of the Supporting Information. As evident from Figure S2a of the Supporting Information, there clearly exists a conduction band offset for configuration A at the CdS–FTO interface, which hinders the flow of electrons toward the FTO side. This is also reflected in the form of enhanced recombination of the charge carriers which is of the order of 10^{20} cm^{-3} s^{-1} at the CdS–FTO interface (Figure S3a, Supporting Information). The configuration B has a very favorable energy band alignment and thus a lower recombination rate (Figure S3b, Supporting Information) for the transfer of electrons through the conduction band and holes through the valence band. This configuration therefore has the highest value of J_{SC} and consequently the power conversion efficiency (η) in the simulation results (Figure S1b, Supporting Information). In spite of this the performance of configuration B in practice is not satisfactory as evident from Table 1. This result therefore suggests the importance of conducting theoretical investigations for optimizing the solar cell structure before fabrication. In terms of the structural configurations C and D are similar; however the simulation results indicate that the performance of configuration C is more unsatisfactory than that of configuration D. The presence of valence band offset at the Cs_2SnI_6–P3HT interface in the energy band diagram of configuration C (shown by dotted circle in Figure S3c, Supporting Information) severely impairs the flow of holes to the collector. As a result the least value of J_{SC} and η is recorded for configuration C among all other configurations. Interestingly, it can be

Table 2. Initial material parameters used in the simulation.

Material parameters	FTO	TiO$_2$	Cs$_2$SnI$_6$	Cu$_2$O
Thickness, t [nm]	500	100	650 (variable)	100
Bandgap, E_g [eV]	3.5	3.2	1.48 (variable)	2.17
Electron affinity, χ [eV]	4.0	4.1	4.01	3.2
Dielectric constant, ϵ_r	9.0	9.0	10.0	7.1
CB effective density of states, N_c [cm^{-3}]	2.2×10^{17}	2.0×10^{18}	2.2×10^{18}	2.5×10^{18}
VB effective density of states, N_c [cm^{-3}]	1.8×10^{17}	1.8×10^{19}	1.8×10^{19}	2.2×10^{18}
Electron mobility, μ_e (cm^2 V^{-1} s^{-1}]	20	20	310	200
Hole mobility, μ_h [cm^2 V^{-1} s^{-1}]	10	10	310	800
Donor concentration, N_d [cm^{-3}]	2.0×10^{17}	1.0×10^{16}	1.0×10^{15}	–
Acceptor concentration, N_a [cm^{-3}]	–	–	1.0×10^{15}	9.0×10^{15}

**ADVANCED
SCIENCE NEWS**

www.advancedsciencenews.com

**ADVANCED
THEORY AND
SIMULATIONS**

www.advtheorysimul.com

Table 3. Shallow and deep level defects used in the simulation.

Description		TiO$_2$	Cs$_2$SnI$_6$	Cu$_2$O
	Type	Neutral	Neutral	Neutral
Shallow	Capture cross section for electrons and holes, σ_e and σ_h [cm^{-2}]	1.0×10^{-15} and 1.0×10^{-15}	2.0×10^{-14} and 2.0×10^{-14}	1.0×10^{-15} and 1.0×10^{-15}
	Energy distribution	VB tail/CB tail	VB tail/CB tail	VB tail/CB tail
	Energy level with respect to E_c/E_v [eV]	0.02 above/0.02 below	0.02 above/0.02 below	0.02 above/0.02 below
	Characteristic energy [eV]	0.01	0.01	0.01
	Total defect density [cm^{-3}]	1.0×10^{15}	1.0×10^{15} (variable)	1.0×10^{15}
Deep	Capture cross section for electrons and holes, σ_e and σ_h [cm^{-2}]	1.0×10^{-15} and 1.0×10^{-15}	2.0×10^{-14} and 2.0×10^{-14}	1.0×10^{-15} and 1.0×10^{-15}
	Energy distribution	Gaussian	Gaussian	Gaussian
	Energy level with respect to E_c/E_v [eV]	1.1 above/1.1 below	0.6 above/0.6 below	0.8 above/0.8 below
	Characteristic energy [eV]	0.1	0.1	0.1
	Total defect density [cm^{-3}]	1.0×10^{15}	1.0×10^{15} (variable)	1.0×10^{15}

Table 4. Defect description at the interfaces.

Description	TiO$_2$/Cs$_2$SnI$_6$	Cs$_2$SnI$_6$/Cu$_2$O
Type	Neutral	Neutral
Capture cross section for electrons and holes, σ_e and σ_h [cm^{-2}]	1.0×10^{-15} and 1.0×10^{-15}	1.0×10^{-15} and 1.0×10^{-15}
Energy distribution	Uniform	Uniform
Energy level with respect to E_c/E_v [eV]	0.0 above/0.0 below	0.0 above/0.0 below
Characteristic energy [eV]	0.1	0.1
Total defect density [cm^{-3}]	1.0×10^{17} (variable)	1.0×10^{17} (variable)

noted that p-type semiconducting characteristic of Cs$_2$SnI$_6$ can be detrimental to the performance of the solar cell because of unfavorable band alignment with P3HT hole transport layer. It can also be confirmed from the simulation results that the presence of hole transport material is essential in obtaining a high open-circuit voltage (V_{OC}).

5. Optimization of the Proposed Cs$_2$SnI$_6$ Solar Cell: Results and Discussion

The energy band diagram of the proposed solar cell is shown in **Figure 2**a exhibiting an excellent conduction and valence band alignment favoring the transport of electrons and holes. The charge carrier recombination rate of the solar cell as a function of position is also demonstrated in Figure 2b. It is apparent that the maximum recombination rate of the proposed solar cell ($<10^{19}$ cm^{-3}) is an order smaller than the maximum recombination rate of the configurations A, B, C, and D. The current density–voltage (J–V) characteristic curve and the initial results of the simulation, based on the tabulated inputs in the last section are shown in Figure 2c. These results were obtained considering an energy bandgap of 1.48 eV and a total defect density of 1.0×10^{15} cm^{-3} for both shallow and deep level defects for the Cs$_2$SnI$_6$ material. Also, importantly the defects concentrations at the TiO$_2$/Cs$_2$SnI$_6$ and Cs$_2$SnI$_6$/Cu$_2$O interfaces were assumed to be 1.0×10^{17} cm^{-3} for the simulations. It is also to be noted here that unless otherwise stated, the back contact metal work function was con-

sidered to be flatband during the optimization of the proposed solar cell.

5.1. Effect of Cs$_2$SnI$_6$ Bandgap and Thickness

It has been reported that the direct optical bandgap of Cs$_2$SnI$_6$ material varies from 1.3 to 1.62 eV.[40] Therefore in order to optimize the proposed solar cell the energy bandgap was varied from 1.3 to 1.65 eV, while the thickness was changed from 100 to 1000 nm. It is evident from **Figure 3**a, that the highest V_{OC} is recorded for a thickness greater than 450 nm and an energy bandgap of 1.5 eV. It must also be noted that the V_{OC} is relatively weakly dependent on the thickness of the absorber as compared to the bandgap of the material. This is expected because an increase in bandgap of the perovskite absorber layer implies that the photogenerated electrons and holes are separated by a greater energy barrier thus reducing the possibility of radiative recombination.[45] On the other hand, the maximum value in terms of J_{SC} is obtained for bandgap lower than 1.37 eV and thickness higher than 600 nm as clear from Figure 3b. A thicker absorber layer allows more absorption of photons in a perovskite material because of the long diffusion length of charge carriers. However the absorber layer thickness should be carefully chosen as very thick absorbers increase the possibility of charge carriers being lost due to recombination before they are extracted by the electron and hole transport layers.[46] It is obvious from these results that a thick Cs$_2$SnI$_6$ absorber layer is beneficial for
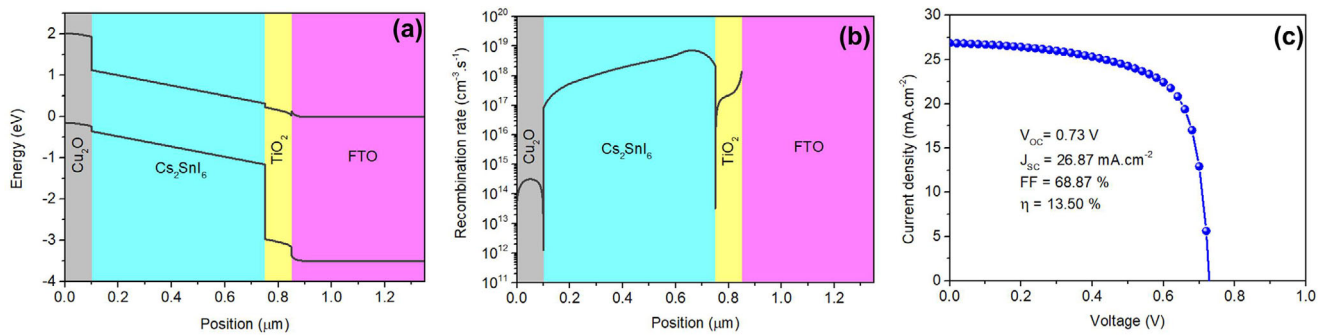
**ADVANCED
SCIENCE NEWS**

www.advancedsciencenews.com

**ADVANCED
THEORY AND
SIMULATIONS**

www.advtheorysimul.com

Figure 2. a) Energy band diagram, b) carrier recombination profile, and c) J–V characteristics of the proposed Cs_2SnI_6 perovskite solar cell.
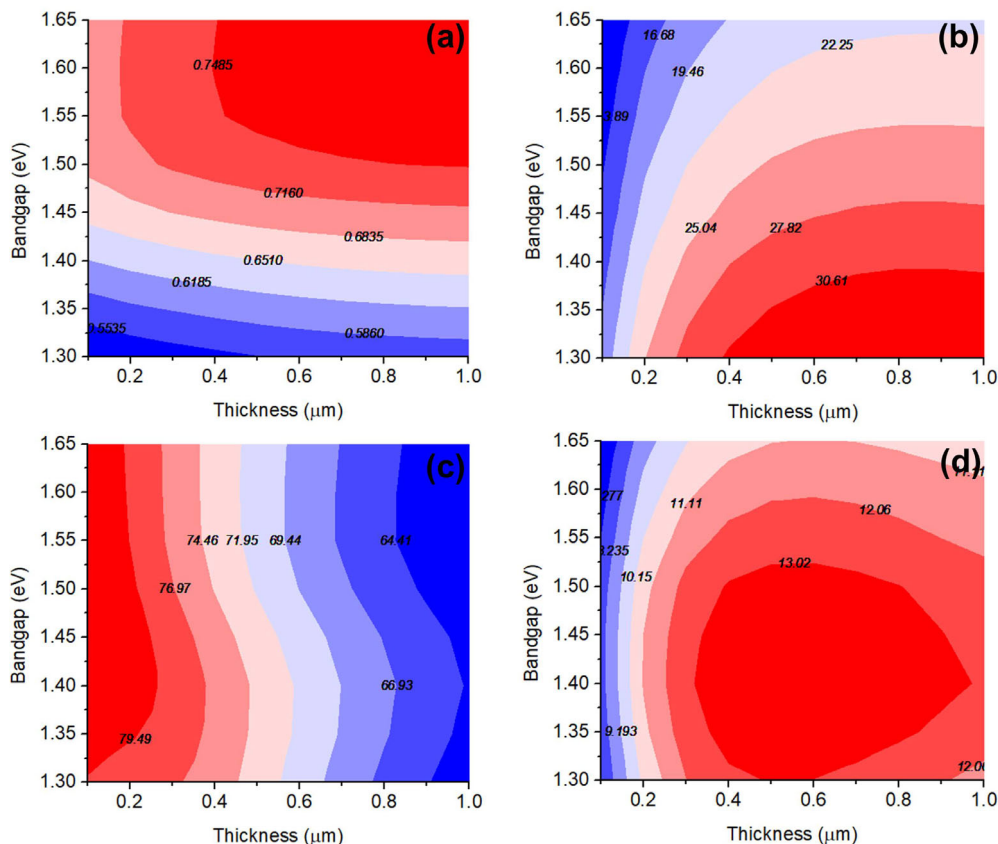

Figure 3. Effect of varying the absorber layer bandgap and thickness on the a) V_{OC}, b) J_{SC}, c) FF, and d) η.

both V_{OC} and J_{SC}. An inspection of Figure 3c also shows that the FF of the cell is independent of the energy bandgap of the absorber material but has a strong dependence on the thickness of the material. This is because an increase in thickness of the absorber corresponds to an increase in the series resistance, which ultimately leads to a decrease in FF of the solar cell.[47] The overall η of the proposed solar cell can be maximized if the bandgap and thickness of Cs_2SnI_6 can be restricted from 1.3 to 1.5 eV and 300 to 900 nm, respectively, as evident from the results of simulation in Figure 3d. The thickness and bandgap optimization results of Cs_2SnI_6 layer suggests that in order to obtain the maximum power conversion efficiency, the energy bandgap

and the thickness of absorber must be 1.40 eV and 600 nm, respectively.

5.2. Effect of Shallow and Deep Level Defects in Cs_2SnI_6

Tap-assisted recombination can occur due to the presence of energy states close to the band edges or in the middle of the energy bandgap. These trap states can significantly alter the carrier mobilities and lifetimes by facilitating electron–hole recombination and weakening the overall performance of the solar cell.[48,49] The shallow acceptor and donor defects in a semiconductor lie close
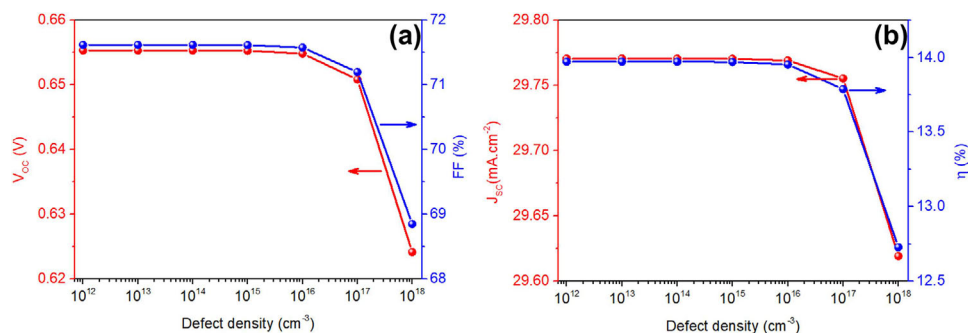
**ADVANCED
SCIENCE NEWS**

www.advancedsciencenews.com

**ADVANCED
THEORY AND
SIMULATIONS**

www.advtheorysimul.com

Figure 4. Effect of varying the shallow defect density of absorber layer on the a) V_{OC} and FF and b) J_{SC} and η.

to the band edges and contribute to the unintentional doping of the semiconductor material due to ionization process at room temperature. The presence of defects inside the lattice such as interstitial defects and ionic vacancies are considered to be the reason to contribute to shallow defect states. In this study the shallow defects inside the absorber are located 0.02 eV below and above the conduction and valence band, respectively. The shallow defects present in Cs_2SnI_6 are neutral in nature with a characteristic energy of 0.01 eV and has an exponential distribution. The capture cross-section of the electrons and the holes used in this study is held constant at 2.0×10^{-14} cm^{-2} for the absorber material. It is evident from the results shown in **Figure 4**a,b that the shallow defect trap density does not have a particularly significant effect in degrading the performance of the solar cell. This is in agreement with other findings that suggest that the shallow defects have negligible influence on the recombination of charge carriers and thus does not hamper the V_{OC} and J_{SC} values to a great extent.[50–52] The results presented herein also suggest that for shallow defect concentrations greater than 10^{17} cm^{-3} the performance of the solar cell starts degrading rapidly because of increased trapping–detrapping mechanism, which ultimately leads to reduced mobility of charge carriers.[53] It must also be emphasized in this regard that Cs_2SnI_6 double perovskite material has proven to be a robust alternative as compared to some other double perovskite materials in terms of the resistance it offers to the decrement in J_{SC} with increase in shallow defect density.[39]

Deep level transient spectroscopy was used to study the defect states and their densities in $CH_3NH_3PbI_3$ perovskite solar cells prepared using two different techniques. The presence of deep level defects was detected in both the samples with trap density of 1.3×10^{15} and 5×10^{15} cm^{-3} located at 0.62 eV.[54] The deep level defects or mid-band defect states considered in this study are located at the mid of the forbidden bandgap at an energy level 0.6 eV above the valence band and 0.6 eV below the conduction band, respectively. The capture cross-sectional area of electrons and holes are considered to be 2.0×10^{-14} cm^{-2} and the total defect density of the traps is varied from 10^{12} to 10^{18} cm^{-3}. In a realistic perovskite solar cell the Gaussian type deep level defects are accountable for charge carrier recombination, limiting the conductivity of the device as well as restricting the effective mobility of the charge carriers due to multiple trapping and liberating processes.[55] Therefore the energy distribution of the neutral defect states in this simulation is also considered to be Gaussian in nature having a characteristic energy of 0.1 eV. The recombi-

nation rate of charge carriers can be expressed by the Shockley–Read–Hall (SRH) model given mathematically as

$$R = \frac{np - n_i^2}{\tau_p \left(n + N_C \exp \left(E_g - E_t \right)/kT \right) + \tau_n \left(p + N_v \exp \left(E_t \right)/kT \right)}$$

(7)

where n is the concentration of electrons, p is concentration of holes, n_i is intrinsic carrier concentration, τ_n is electron lifetime, τ_p is hole lifetime, N_C is conduction band density of states, N_V is valence band density of states, E_g is bandgap energy, E_t is energy trap level, k is Boltzmann constant, and T is temperature. Furthermore the lifetime of the charge carriers is given by the relation

$$\tau = \frac{1}{\sigma v_{th} N_t}$$

(8)

where σ is the capture cross section of the charge carriers, v_{th} is the thermal velocity, and N_t is trap defect concentration.

The results from **Figure 5**a suggests that the V_{OC} and FF of the solar cell remains fairly constant if the deep defect density is restricted below 10^{15} cm^{-3}, beyond which it falls over sharply. It is also evident from Figure 5b that J_{SC} sharply declines only after the defect density exceeds 10^{16} cm^{-3}, but the overall power conversion efficiency of the proposed solar cell exhibits a rapid decrease if the defect density increases beyond 10^{15} cm^{-3}. The decrease in V_{OC} and J_{SC} of the proposed solar cell is because of the decline in charge carrier lifetime (τ) from 5000 ns to 5 ps when the defect density is increased from 10^{12} to 10^{18} cm^{-3}, which also corresponds to a decrease in diffusion length (L) of electrons and holes from 63.2 μm to 63.2 nm. Therefore nonradiative (SRH) recombination of charge carriers inside the perovskite material must be avoided in order to practically realize a device with high efficiency by preferably limiting the concentration of deep defects below 10^{15} cm^{-3}.

5.3. Effect of Interfacial Defects

Interfacial defects impair the performance of the device to a large extent because of the interaction of electron and hole transport materials with the perovskite precursor during the deposition process resulting in the formation of grain boundaries.[56] The performance of the solar cell can be restored to some extent by
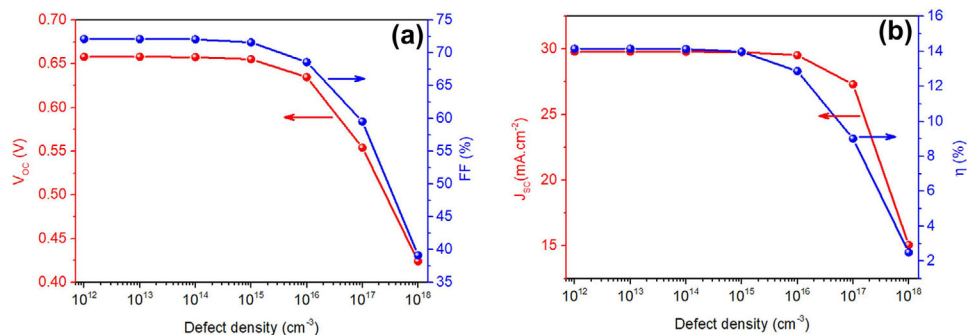
**ADVANCED
SCIENCE NEWS**

www.advancedsciencenews.com

**ADVANCED
THEORY AND
SIMULATIONS**

www.advtheorysimul.com

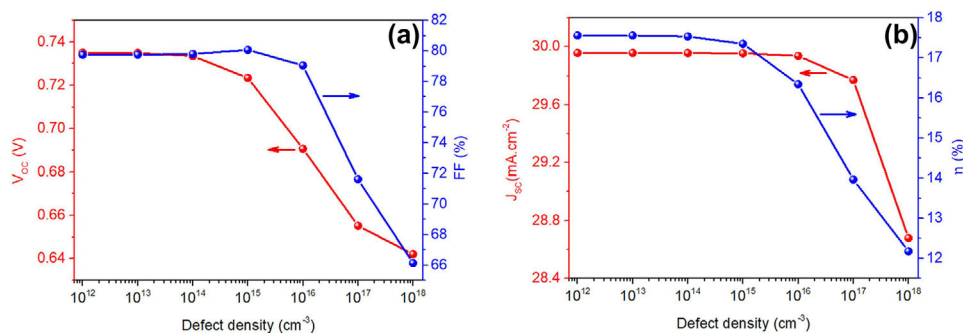**Figure 5.** Effect of varying the deep defect density of absorber layer on the a) V_{OC} and FF and b) J_{SC} and η.

Figure 6. Effect of varying the total defect density at the TiO_2/Cs_2SnI_6 interface on a) V_{OC} and FF and b) J_{SC} and η.

inhibiting interfacial charge carrier recombination by passivation of trap states thereby restoring the V_{OC} of the cell.[57–59] In this investigation the TiO_2/Cs_2SnI_6 and Cs_2SnI_6/Cu_2O interfaces are characterized by neutral defects having uniform distribution with capture cross section of 10^{-15} cm^{-3} for electrons and holes. The defect density at the interfaces was varied from 10^{12} to 10^{18} cm^{-3} and the changes in the electrical parameters were recorded. **Figure 6**a clearly shows that the V_{OC} of the cell almost immediately shows a sharp decrease when the defect concentration increases beyond 10^{18} cm^{-3}. This result clearly suggests that nonradiative recombination originating from the interface of the electron transport material and perovskite is the reason for the most significant V_{OC} loss in perovskite solar cells, in agreement with earlier reports.[60,61] On the other hand, the impact of TiO_2/Cs_2SnI_6 interfacial defect concentration is not so pronounced in case of

J_{SC} (Figure 6b), as an insignificant decline is noted at densities greater than 10^{16} cm^{-3}. It is evident from these results that the power conversion efficiency in this case is largely governed by the V_{OC} of the solar cell. Interestingly, at the Cs_2SnI_6/Cu_2O interface, it was found that increasing the defect concentration from 10^{12} to 10^{18} cm^{-3} had a negligible effect on the V_{OC} and J_{SC} of the proposed solar cell (**Figure 7**a,b). This is in agreement with similar investigations carried out in the past where it was reported that the electron transport/perovskite layer induces more interfacial recombination compared to perovskite/hole transport layer.[62,63] This argument is in general however applicable for perovskite and charge transport materials exhibiting no energy band misalignment at their interfaces.

The important parameters which dictate the performance of the solar cell were optimized the results of which are summa-
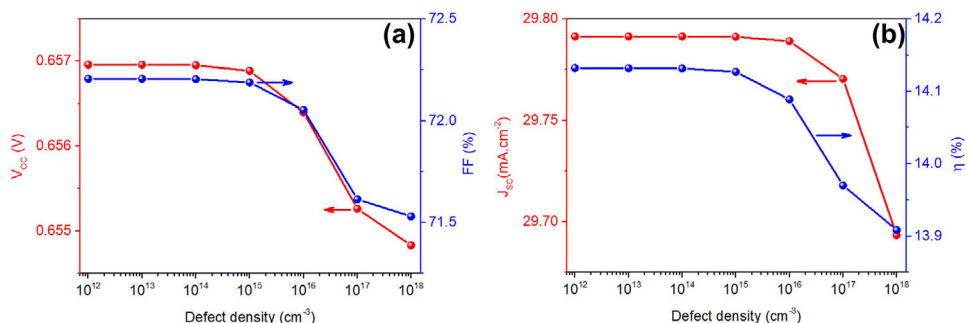
Figure 7. Effect of varying the total defect density at the Cs_2SnI_6/Cu_2O interface on a) V_{OC} and FF and b) J_{SC} and η.

**ADVANCED
SCIENCE NEWS**

www.advancedsciencenews.com

**ADVANCED
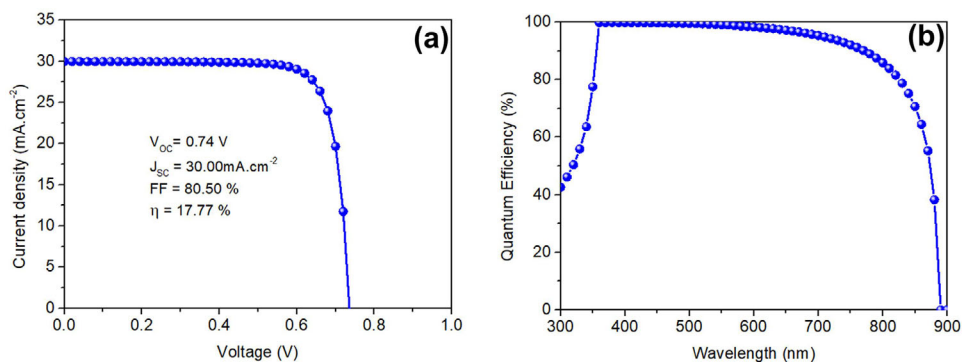THEORY AND
SIMULATIONS**

www.advtheorysimul.com

Figure 8. a) $J–V$ characteristics and b) quantum efficiency of the optimized Cs_2SnI_6 perovskite solar cell.

Table 5. Optimum parameters of the proposed solar cell.

Parameters	Values
Cs_2SnI_6 thickness [nm]	600
Cs_2SnI_6 energy bandwidth [eV]	1.4
Absorber layer-shallow defect density [cm^{-3}]	$\leq 10^{17}$
Absorber layer-deep defect density [cm^{-3}]	$\leq 10^{15}$
TiO_2/Cs_2SnI_6 interface-total defect density [cm^{-3}]	$\leq 10^{15}$
Cs_2SnI_6/Cu_2O interface-total defect density [cm^{-3}]	$\leq 10^{18}$

rized in **Table 5**. In the light of the discussions above it should be ensured that in order to extract the best performance from the Cs_2SnI_6 perovskite solar cell, the thickness of the absorber must be 600 nm and the energy bandgap 1.4 eV. It is also to be assured that the shallow defect density inside the absorber material is restricted to less than 10^{17} cm^{-3} and the deep defect concentration is limited to 10^{15} cm^{-3}. Unlike the hole transport layer–perovskite interface, the interface between electron transport material and the perovskite is the reason for most open-circuit voltage loss in the device and the total defect density at this interface should be confined to 10^{15} cm^{-3} in order to extract the optimum performance from the Cs_2SnI_6 perovskite solar cell. The $J–V$ characteristic curve of the optimized solar cell is shown in **Figure 8**a with all the realistically achievable electrical parameters. The spectral response from Figure 8b shows that the proposed solar cell is highly responsive to visible light illumination with the ability to convert the energy of the photons throughout almost the entire visible range to electrical energy.

5.4. Effect of Metal Back Contact

It should at this point be highlighted that the investigations carried out on the proposed solar cell till now assumed that the back contact was flatband, which meant that the effect of the work function of the anode material was ignored. In a practical solar cell device however the work function of the anode plays a crucial role in regulating the power conversion efficiency of a solar cell. The metal contact and hole transport material interface in practice exhibits ohmic or rectifying characteristics impeding the transport of holes.[64–66] Therefore, various back metal con-

tacts with different work functions were studied, which can be employed as anode materials in the proposed Cs_2SnI_6 perovskite solar cell. The potential energy barrier at the hole transport material and back metal contact interface is governed by the relation

$$V_b = \frac{E_g}{q} + \chi - \phi_m \qquad (9)$$

where χ is the electron affinity and ϕ_m is the metal work function.[67] When the work function of the back metal increases the potential energy barrier decreases, facilitating the transport and collection of holes at the anode thereby leading to an increase in efficiency. The different metals used in the simulations were Al, Ni, Cr, Cu, Ag, Au, and Ni with work functions 4.3, 4.33, 4.5, 4.7, 4.74, 5.1, and 5.15 eV were used in this investigation.[43,68–70] As apparent from **Figure 9**a, the V_{OC} of the solar cell increases with the increase in work function of the metals below 4.7 eV and saturates thereafter.[71] The variation in the J_{SC}, on the other hand is not so distinct which can be observed from Figure 9b. The FF and η of the proposed solar cell (Figure 9c,d) also increases with the increase in the work function of the back metal contact. It was found from the analysis that Au and Ni were good candidates as hole selective contacts, which can be employed in conjunction with Cu_2O hole transport material in a Cs_2SnI_6 solar cell to achieve over 17% power conversion efficiency. In fact it was apparent from the results of the simulation that metals having work function less than 5.1 eV formed Schottky barrier contact with Cu_2O hindering the transport of holes. On the other hand for metals having work functions greater than 5.1 eV the metal–semiconductor junction acted as an ohmic contact favoring the transfer of holes.

6. Conclusion

Numerical simulation was conducted to investigate the performance of a novel double perovskite solar cell utilizing Cs_2SnI_6 absorber material. The 1D SCAPS program was used to study the fully inorganic, nontoxic $FTO/TiO_2/Cs_2SnI_6/Cu_2O$ solar cell architecture. The proposed double perovskite solar cell could achieve an open-circuit voltage of 0.74 V, short-circuit current density of 30 mA cm^{-2}, fill factor of 80.5%, and a power conversion efficiency of 17.77%. It was found that the performance of the solar cell was highly dependent on the thickness and bandgap
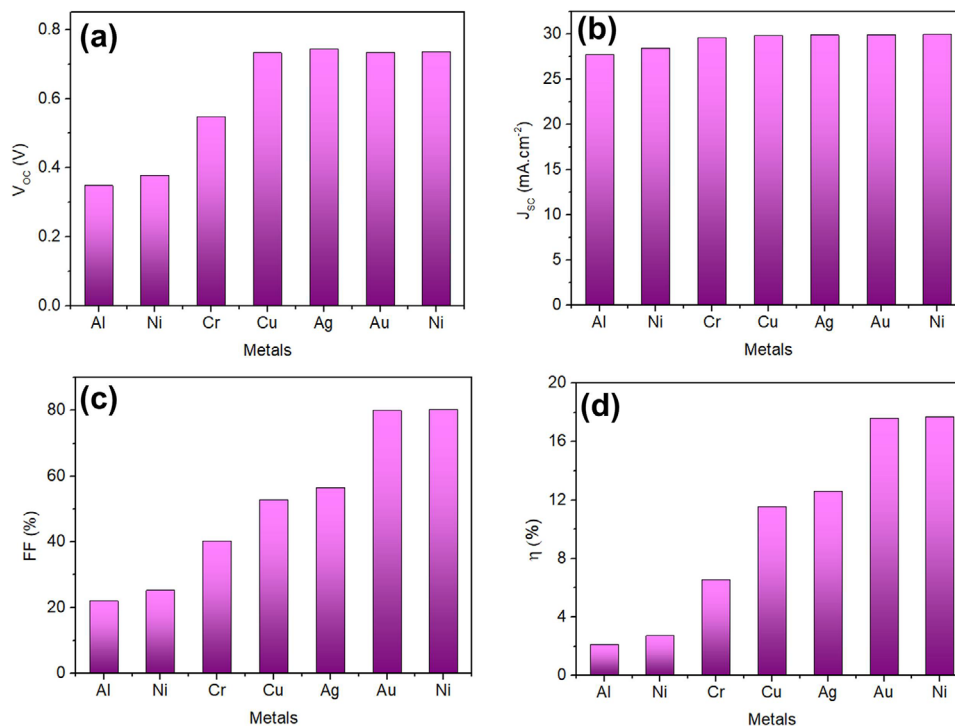
Figure 9. Variation of a) V_{OC}, b) J_{SC}, c) FF, and d) η of the Cs_2SnI_6 perovskite solar cell for back contact metals with different work function.

of the absorber layer and to extract the best performance from the device the thickness of the Cs_2SnI_6 should be 600 nm with an energy bandgap of 1.4 eV. As expected the shallow defect states inside the absorber material had a negligible control in dictating the performance of the device unless the defect concentration exceeded an extremely high value of 10^{17} cm^{-3}. A similar behavior was observed for Cs_2SnI_6/Cu_2O interfacial characteristics wherein we found insignificant dependence of device performance on the defect density if the total concentration could be limited below 10^{18} cm^{-3}. The results of the theoretical investigation also suggest that the performance of the proposed solar cell is strongly governed by the deep level nonradiative recombination centers present in the perovskite material and the TiO_2/Cs_2SnI_6 interfacial defect concentration, both of which must be restricted below 10^{15} cm^{-3} to achieve a high efficiency device. The role of back contact work function is also critical factor and it was established that the back metal should have a work function greater than or equal to 5.1 eV to realize practically achievable conversion efficiency greater than 17%.

Supporting Information

Supporting Information is available from the Wiley Online Library or from the author.

Acknowledgements

Conflict of Interest

The author declares no conflict of interest.

Data Availability Statement

The data that support the findings of this study are available in the supplementary material of this article.

Keywords

[1] W. Zhang, G. E. Eperon, H. J. Snaith, *Nat. Energy* **2016**, *1*, 16048.

[2] N.-G. Park, *Mater. Today* **2015**, *18*, 65.

[3] M. A. Green, A. Ho-Baillie, H. J. Snaith, *Nat. Photonics* **2014**, *8*, 506.

[4] S. D. Stranks, H. J. Snaith, *Nat. Nanotechnol.* **2015**, *10*, 391.

[5] L. Xu, C. Zhang, X. Feng, W. Lv, Z. Huang, W. Lv, C. Zheng, G. Xing, W. Huang, R. Chen, *J. Mater. Chem. A* **2021**, *9*, 16943.

[6] W. Ke, C. C. Stoumpos, I. Spanopoulos, L. Mao, M. Chen, M. R. Wasielewski, M. G. Kanatzidis, *J. Am. Chem. Soc.* **2017**, *139*, 14800.

[7] S. J. Lee, S. S. Shin, Y. C. Kim, D. Kim, T. K. Ahn, J. H. Noh, J. Seo, S. I. Seok, *J. Am. Chem. Soc.* **2016**, *138*, 3974.

[8] M. Zhang, Z. Zhang, H. Cao, T. Zhang, H. Yu, J. Du, Y. Shen, X.-L.i Zhang, J. Zhu, P. Chen, M. Wang, *Mater. Today Energy* **2022**, *23*, 100891.

**ADVANCED
SCIENCE NEWS**

www.advancedsciencenews.com

**ADVANCED
THEORY AND
SIMULATIONS**

www.advtheorysimul.com

[9] F. Wang, X. Jiang, H. Chen, Y. Shang, H. Liu, J. Wei, W. Zhou, H. He, W. Liu, Z. Ning, *Joule* **2018**, *2*, 2732.

[10] B.-B. Yu, Z. Chen, Y. Zhu, Y. Wang, B. Han, G. Chen, X. Zhang, Z. Du, Z. He, *Adv. Mater.* **2021**, *33*, 2102055.

[11] X. Jiang, F. Wang, Q.i Wei, H. Li, Y. Shang, W. Zhou, C. Wang, P. Cheng, Q.i Chen, L. Chen, Z. Ning, *Nat. Commun.* **2020**, *11*, 1245.

[12] N. K. Noel, S. D. Stranks, A. Abate, C. Wehrenfennig, S. Guarnera, A.-A. Haghighirad, A. Sadhanala, G. E. Eperon, S. K. Pathak, M. B. Johnston, A. Petrozza, L. M. Herz, H. J. Snaith, *Energy Environ. Sci.* **2014**, *7*, 3061.

[13] M. H. Kumar, S. Dharani, W. L. Leong, P. P. Boix, R. R. Prabhakar, T. Baikie, C. Shi, H. Ding, R. Ramesh, M. Asta, M. Graetzel, S. G. Mhaisalkar, N. Mathews, *Adv. Mater.* **2014**, *26*, 7122.

[14] K. Nishimura, M. A. Kamarudin, D. Hirotani, K. Hamada, Q. Shen, S. Iikubo, T. Minemoto, K. Yoshino, S. Hayase, *Nano Energy* **2020**, *74*, 104858.

[15] S. Ullah, J. Wang, P. Yang, L. Liu, J. Khan, S.-E. Yang, T. Xia, H. Guo, Y. Chen, *Sol. RRL* **2021**, *5*, 2000830.

[16] A. Raj, M. Kumar, A. Anshul, *Phys. Status Solidi* **2022**, *219*, 2200425.

[17] M. Rasukkannu, D. Velauthapillai, P. Vajeeston, *Mater. Lett.* **2018**, *218*, 233.

[18] S. Ullah, J. Wang, M. H. Alvi, R. Chang, P. Yang, L. Liu, S.-E. Yang, T. Xia, H. Guo, Y. Chen, *Int. J. Energy Res.* **2021**, *45*, 1720.

[19] S. Ullah, S. Ullah, J. Wang, S.-E. Yang, T. Xia, H. Guo, Y. Chen, *Semicond. Sci. Technol.* **2020**, *35*, 125027.

[20] F. J. Amaya Suazo, S. Shaji, D. A. Avellaneda, J. A. Aguilar-Martínez, B. Krishnan, *Sol. Energy* **2020**, *207*, 486.

[21] X. Qiu, Y. Jiang, H. Zhang, Z. Qiu, S. Yuan, P. Wang, B. Cao, *Phys. Status Solidi RRL* **2016**, *10*, 587.

[22] X. Qiu, B. Cao, S. Yuan, X. Chen, Z. Qiu, Y. Jiang, Q. Ye, H. Wang, H. Zeng, J. Liu, M. G. Kanatzidis, *Sol. Energy Mater. Sol. Cells* **2017**, *159*, 227.

[23] Y. Jiang, H. Zhang, X. Qiu, B. Cao, *Mater. Lett.* **2017**, *199*, 50.

[24] J. Zhang, S. Li, P. Yang, W. Liu, Y. Liao, *J. Mater. Sci.* **2018**, *53*, 4378.

[25] H. Tsai, R. Asadpour, J.-C. Blancon, C. C. Stoumpos, O. Durand, J. W. Strzalka, B.o Chen, R. Verduzco, P. M. Ajayan, S. Tretiak, J. Even, M. A. Alam, M. G. Kanatzidis, W. Nie, A. D. Mohite, *Science* **2018**, *360*, 67.

[26] D.-Y. Son, J.-W. Lee, Y. J.i Choi, I.n-H. Jang, S. Lee, P. J. Yoo, H. Shin, N. Ahn, M. Choi, D. Kim, N.-G. Park, *Nat. Energy* **2016**, *1*, 16081.

[27] N. Ahn, D.-Y. Son, I.-H. Jang, S. M. Kang, M. Choi, N.-G. Park, *J. Am. Chem. Soc.* **2015**, *137*, 8696.

[28] T. A. Berhe, W.-N. Su, C.-H. Chen, C.-J. Pan, J.-H. Cheng, H.-M. Chen, M.-C. Tsai, L.-Y. Chen, A. A. Dubale, B.-J. Hwang, *Energy Environ. Sci.* **2016**, *9*, 323.

[29] W. Tress, N. Marinova, T. Moehl, S. M. Zakeeruddin, M. K. Nazeeruddin, M. Grätzel, *Energy Environ. Sci.* **2015**, *8*, 995.

[30] M. M. Tavakoli, M. Saliba, P. Yadav, P. Holzhey, A. Hagfeldt, S. M. Zakeeruddin, M. Grätzel, *Adv. Energy Mater.* **2019**, *9*, 1802646.

[31] N.-G. Park, M. Grätzel, T. Miyasaka, K. Zhu, K. Emery, *Nat. Energy* **2016**, *1*, 16152.

[32] J.-W. Lee, D.-H. Kim, H.-S. Kim, S.-W. Seo, S. M. Cho, N.-G. Park, *Adv. Energy Mater.* **2015**, *5*, 1501310.

[33] Y. Yuan, J. Huang, *Acc. Chem. Res.* **2016**, *49*, 286.

[34] E. L. Unger, E. T. Hoke, C. D. Bailie, W. H. Nguyen, A. R. Bowring, T. Heumüller, M. G. Christoforo, M. D. Mcgehee, *Energy Environ. Sci.* **2014**, *7*, 3690.

[35] S. Porwal, M. Paul, H. Dixit, S. Mishra, T. Singh, *Adv. Theory Simul.* **2022**, *5*, 2200207.

[36] A. Chauhan, A. Oudhia, A. K. Shrivastav, *J. Mater. Sci.* **2022**, *33*, 1670.

[37] M. Burgelman, P. Nollet, S. Degrave, *Thin Solid Films* **2000**, *361–362*, 527.

[38] A. Tara, V. Bharti, S. Sharma, R. Gupta, *Opt. Mater.* **2021**, *119*, 111362.

[39] D. Pal, S. Das, *Opt. Mater.* **2020**, *108*, 110453.

[40] X. Nairui, T. Yehua, Q. Yali, L. Duoduo, W. Ke-Fan, *Sol. Energy* **2020**, *204*, 429.

[41] J. Wu, Z. Zhao, Y. Zhou, *Sci. Rep.* **2022**, *12*, 935.

[42] B. Lee, C. C. Stoumpos, N. Zhou, F. Hao, C. Malliakas, C.-Y.u Yeh, T. J. Marks, M. G. Kanatzidis, R. P. H. Chang, *J. Am. Chem. Soc.* **2014**, *136*, 15379.

[43] Y. Raoui, H. Ez-Zahraouy, N. Tahiri, O. El Bounagui, S. Ahmad, S. Kazim, *Sol. Energy* **2019**, *193*, 948.

[44] C. Zuo, L. Ding, *Small* **2015**, *11*, 5528.

[45] S. Bishnoi, S. K. Pandey, *IET Optoelectron.* **2018**, *12*, 185.

[46] D. Pal, S. Das, *Mater. Today Proc.* **2020**, *46*, 6367.

[47] A. Bag, R. Radhakrishnan, R. Nekovei, R. Jeyakumar, *Sol. Energy* **2020**, *196*, 177.

[48] D. Kumar, S. Porwal, T. Singh, *Emergent. Mater.* **2022**, *5*, 987.

[49] T. Singh, S. Öz, A. Sasinska, R. Frohnhoven, S. Mathur, T. Miyasaka, *Adv. Funct. Mater.* **2018**, *28*, 1706287.

[50] S. R. Raga, Y. Qi, *J. Phys. Chem. C* **2016**, *120*, 28519.

[51] W.-J. Yin, T. Shi, Y. Yan, *Adv. Mater.* **2014**, *26*, 4653.

[52] W.-J. Yin, T. Shi, Y. Yan, *Appl. Phys. Lett.* **2014**, *104*, 063903.

[53] H. Jin, E. Debroye, M. Keshavarz, I. G. Scheblykin, M. B. J. Roeffaers, J. Hofkens, J. A. Steele, *Mater. Horiz.* **2020**, *7*, 397.

[54] S. Heo, G. Seo, Y. Lee, D. Lee, M. Seol, J. Lee, J.-B. Park, K. Kim, D.-J. Yun, Y. S.u Kim, J. K. Shin, T. K. Ahn, M. K. Nazeeruddin, *Energy Environ. Sci.* **2017**, *10*, 1128.

[55] J. M. Ball, A. Petrozza, *Nat. Energy* **2016**, *1*, 16149.

[56] F. Wang, S. Bai, W. Tress, A. Hagfeldt, F. Gao, *npj Flexible Electron* **2018**, *2*, 22.

[57] V. Sarritzu, N. Sestu, D. Marongiu, X. Chang, S. Masi, A. Rizzo, S. Colella, F. Quochi, M. Saba, A. Mura, G. Bongiovanni, *Sci. Rep.* **2017**, *7*, 44629.

[58] M. Alidaei, M. Izadifard, M. E. Ghazi, F. A. Roghabadi, V. Ahmadi, *J. Mater. Sci.* **2019**, *30*, 6936.

[59] H. Sun, D. Xie, Z. Song, C. Liang, L. Xu, X. Qu, Y. Yao, D. Li, H. Zhai, K. Zheng, Y. Cui, Y. Zhao, *ACS Appl. Mater. Interfaces* **2020**, *12*, 22853.

[60] S. Mahesh, J. M. Ball, R. D. J. Oliver, D. P. Mcmeekin, P. K. Nayak, M. B. Johnston, H. J. Snaith, *Energy Environ. Sci.* **2020**, *13*, 258.

[61] M. Daboczi, I. Hamilton, S. Xu, J. Luke, S. Limbu, J. Lee, M. A. Mclachlan, K. Lee, J. R. Durrant, I. D. Baikie, J.i-S. Kim, *ACS Appl. Mater. Interfaces* **2019**, *11*, 46808.

[62] M. Stolterfoht, P. Caprioglio, C. M. Wolff, J. A. Márquez, J. Nordmann, S. Zhang, D. Rothhardt, U. Hörmann, Y. Amir, A. Redinger, L. Kegelmann, F. Zu, S. Albrecht, N. Koch, T. Kirchartz, M. Saliba, T. Unold, D. Neher, *Energy Environ. Sci.* **2019**, *12*, 2778.

[63] S. Rai, B. K. Pandey, D. K. Dwivedi, *Opt. Mater.* **2020**, *100*, 109631.

[64] G. K. Gupta, A. Dixit, *Int. J. Energy Res.* **2020**, *44*, 3724.

[65] K. Deepthi Jayan, V. Sebastian, *Int. J. Energy Res.* **2021**, *45*, 16618.

[66] K. Shivesh, I. Alam, A. K. Kushwaha, M. Kumar, S. V. Singh, *Int. J. Energy Res.* **2022**, *46*, 6045.

[67] P. K. Patel, *Sci. Rep.* **2021**, *11*, 3082.

[68] A.-A. Kanoun, M. B. Kanoun, A. E. Merad, S. Goumri-Said, *Sol. Energy* **2019**, *182*, 237.

[69] L. Lin, L. Jiang, P. Li, H. Xiong, Z. Kang, B. Fan, Y.u Qiu, *Sol. Energy* **2020**, *198*, 454.

[70] D. Jayan K, V. Sebastian, J. Kurian, *Sol. Energy* **2021**, *221*, 99.

[71] K. Deepthi Jayan, V. Sebastian, *Sol. Energy* **2021**, *217*, 40.